TITLE

Octopamine signals coordinate the spatial pattern of presynaptic machineries in the *Drosophila* mushroom bodies

Hongyang Wu [1,6], Sayaka Eno [1,3,6], Kyoko Jinnai [2], Yoh Maekawa [3], Kokoro Saito [1], Ayako Abe [1], Darren W Williams [4], Nobuhiro Yamagata [1,5], Shu Kondo [2], Hiromu Tanimoto [1,3,7,*]

[1] Graduate School of Life Sciences, Tohoku University, Sendai, Japan.
[2] Department of Biological Science and Technology, Tokyo University of Science, Tokyo, Japan.
[3] Department of Biology, Faculty of Science, Tohoku University, Sendai, Japan.
[4] Centre of Developmental Neurobiology, King's College London, London, United Kingdom.
[5] Department of Life Science, Graduate School of Engineering Science, Akita University, Akita, Japan.
[6] These authors contributed equally.
[7] Lead contact.
*Correspondence: hiromut@m.tohoku.ac.jp (H.T.)

SUMMARY

Neurons need to adjust synaptic output according to the targets. However, the intracellular heterogeneity of synaptic machinery is scarcely reported in the central nervous system, and its regulatory mechanism remain unknown. Applying the CRISPR/Cas9-mediated split-GFP tagging, we devised cell-type specific fluorescent labeling of the endogenous active zone scaffold protein, Bruchpilot (Brp). This technology enabled the quantification of intracellular diversity of presynaptic structures within the Kenyon cells of the *Drosophila* mushroom bodies. We found that the accumulation of Brp at active zones is strikingly heterogenous among the compartments of Kenyon cell axon terminals. Mechanistically, the localized octopaminergic signaling along Kenyon cell terminals regulate the Brp heterogeneity via Octβ2R and cAMP signaling. We further found that acute food deprivation reduced the compartmental heterogeneity of Brp accumulation in an octopaminergic signaling-dependent manner. This synaptic regulation explains how the mushroom body integrates changing physiological states.

KEY WORDS

Split-GFP; mushroom bodies; Kenyon cell; presynaptic active zone; synaptic heterogeneity; compartments; octopamine; stress; cAMP signaling

INTRODUCTION

The molecular composition of chemical synapses determines the function of neurons, and therefore exhibits a remarkable diversity among cell types [1,2]. Studies in the motor neuron demonstrated that presynaptic molecular assemblies are highly heterogeneous even within a single cell [3,4]. Critically, this structural heterogeneity is correlated with synaptic functions such as release probability [5–7]. Given that a single neuron in the

central nervous system (CNS) synapses onto multiple target cells, such intracellular synaptic heterogeneity could generate complex computation of the circuit. However, the regulatory mechanisms of such synaptic heterogeneity in central neurons are largely unknown.

Neurons projecting to the *Drosophila* mushroom bodies (MBs) can serve as an excellent model system to study intracellular synaptic heterogeneity. Kenyon cells (KCs), the major MB intrinsic neurons, synapse onto five sets of post-synaptic partners in spatially segregated compartments [8,9]. Postsynaptic MB output neurons (MBONs) have distinct and compartmentalized dendrites within the MB lobes [9], and their activities collectively determine the MB output [10–14]. The compartmental distinctions in presynaptic assemblies within KCs are likely to be critical in controlling MB-guided behaviors.

We here aim to characterize the intracellular diversity of presynaptic structures in a KC-specific manner. Brp, the homolog of ELKS/CAST/ERC, is a major scaffold protein accumulated at active zones (AZs) and the main component of electron-dense projections decorating AZs [15–18]. Brp clusters determine functional characteristics of synapses such as the release probability of synaptic vesicles [5–7], therefore their structures serve as a proxy for estimating the synapse function. As with other neuropils in the central nervous system, MBs are composed of densely packed synapses originating from different types of neurons [19,20]. Therefore, it is challenging to characterize specific endogenous synapse proteins only in the target neuron without super-resolution microscopy [21,22]. Inspired by recent advances in *Drosophila* genetics to label endogenous Brp in designated cell types [23,24], we took advantage of the CRISPR/Cas9-mediated split-GFP tagging strategy for this purpose [25,26]. Profiling the character of individual Brp clusters only within KCs revealed heterogenous Brp accumulation along the MB compartments. Here we report the dynamics of this intracellularly heterogeneous AZ structure and approach its supervising regulatory mechanisms.

RESULTS

Cell-type specific visualization of endogenous active zone scaffold proteins Brp

Chemical tagging using Brp::SNAP [27] suggests endogenous Brp localizes heterogeneously within the MB (Figure S1), which is constituted by pre-synapses of various cell types (Figure S2). To visualize endogenous Brp in designated cell types, we inserted the GFP_{11} fragment (the eleventh β-strand of the super-folder GFP) just prior to the stop codon of *brp* using CRISPR/Cas9. The self-assembly and reconstitution of GFP is induced by expressing the GFP_{1-10} fragments using the GAL4/UAS system (Figure 1A).

We validated this system with GAL4 driver lines that label 7 different MB-projecting neuronal populations: 3 KC subtypes, 2 dopamine neuron clusters (PPL1 and PAM) and 2 single interneurons (DPM and APL neurons) [9,28] (see STAR★METHOD for driver information). Confocal microscopy detected reconstituted GFP (rGFP) signals only at restricted areas, in contrast to the dense signals in Brp::SNAP or Anti-Brp immunostaining (Figure 1B, Figure S1). The Brp::rGFP signal appeared as individual puncta and matched the areas of axon terminals of the cell types (Figure 1B). Especially, Brp was labeled at single-cell resolution for the APL and DPM neuron [8,29]. Strikingly, the Brp::rGFP signal intensity appeared to be heterogenous along the axon

terminals of KCs (Figure 1B). Since individual KCs arborize onto the entire lobe structure, these results suggest distinct accumulations of Brp intracellularly.

To test whether Brp::rGFP labels dynamic synaptic structures, we benchmarked its performance with different live-imaging contexts. The axon arborizations of pleural muscle motor neurons (PM-Mns) can be imaged on the abdominal body wall during pupal development [30]. Live-imaging Brp::rGFP in the PM-Mn revealed the formation of individual clusters at 48 hours after puparium formation and the increasing density in the same branch following two days (Figure 1C). We further visualized Brp::rGFP dynamics in the ex-vivo preparation of the larval brain, and found multiple fusion and fission events of Brp clusters in the MB calyx (Figure 1D). These results are consistent with the AZ assembly through liquid-liquid phase separation [31] and demonstrated the immense potential to visualize the dynamics of endogenous AZ structures.

Intracellular active zone heterogeneity among MB compartments

To quantify the presynaptic Brp heterogeneity we observed in KCs (Figure 1B), an image-processing pipeline was developed to better characterize the signal intensity (total grey value) of individual Brp::rGFP puncta. Optimizing the parameter combination of 3D image deconvolution [32,33] and spot segmentation enabled to resolve Brp::rGFP clusters that represent single AZs using conventional confocal microscopy [34]. We found that Brp::rGFP accumulation was heterogeneous among KC compartments, and it was especially pronounced in γ KCs (Figure 2A, Figure S3). The median Brp::rGFP signal intensity in the γ5 compartment was nearly three times as intense as that in γ1 (Figure 2C). These results suggest that individual KCs tune their presynaptic structures according to compartments (Figure 2B).

As different MB compartments are functionally coordinated and integrate internal states such as nutritional states, sleep need and aging [10,35–39], we examined whether KCs adapt the synaptic structures upon physiological changes. We quantified the median intensity of Brp::rGFP puncta in each compartment and calculated the variance of the 5 compartments as a measure of compartmental heterogeneity (Figure 2D). Strikingly, the compartmental heterogeneity in γ KCs significantly decreased upon food deprivation for 48 hours (Figure 2E, Figure S6F). In contrast, we did not find a significant effect by aging for 30 d (Figure S5). These results suggest that acute stress can drive local adjustment of AZ structure within KCs, reflecting reorganized compartmental activities.

Associations of Ca^{2+} channel and Brp clusters

In motor neurons, Brp is well characterized to serve as a scaffold protein accumulating synapse proteins such as voltage-gated Ca^{2+} channels [15,17,40]. Therefore, we hypothesized if Brp heterogeneity in γ KCs reflects the Ca^{2+} channel enrichment at AZs. To test the hypothesis, we double-labelled the endogenous α subunit of the voltage-gated Ca^{2+} channel, Cacophony (Cac) and Brp by Cac::sfGFP [6] and Brp::SNAP, respectively. We found that Cac::sfGFP and Brp::SNAP signals were co-localized in the γ lobe (Figure 3A-3B) and their intensities were correlated in Brp-positive areas (Figure 3C-E, Figure S4).

This correlation between Brp and Cac clusters suggest that the Ca^{2+} concentration is differentially set along the γ KCs. To measure the basal Ca^{2+} concentration nearby AZs, we expressed Brp^{short}::mCherry::GCaMP6s, a ratiometric

141 Ca^{2+} sensor fused to mCherry and truncated Brp (Figure 3F) [41], in KCs. We found that
142 basal GCaMP signals were compartmentally distinct and gradually increased towards
143 the γ5 compartment (Figure 3F). This compartmental pattern of GCaMP signals nicely
144 mirrored the Brp heterogeneity. Taken together the colocalization of Brp and Cac, these
145 results suggest that the Brp accumulation per AZ is set compartmentally, differentiating
146 the basal Ca^{2+} influx via Ca^{2+} channels at AZs [42].
147
148 **Octopamine input underlies the Brp compartmental heterogeneity**
149 Each compartment receives dopamine projections from structurally and functionally
150 distinct subsets of dopaminergic neurons (Figure 3A) [9]. We therefore examined whether
151 dopamine inputs determine the compartmental Brp accumulation by knocking-down
152 dopamine receptors (DopR1, DopR2 and D2R) in KCs using RNA interference (RNAi)
153 [43,44]. None of these disruptions showed a significant effect on the compartmental
154 heterogeneity (Figure 4B, Figure S6A).
155 The octopaminergic neurons (OANs), particularly OA-VPM3 and OA-VPM4
156 neurons, are known to project to the MB and concentrate their innervations in the γ1
157 compartment [9,45]. We characterized presynaptic components of OA-VPM3/4 visualized
158 by Brp::rGFP and nSyb::CLIP (neuronal synaptobrevin, nSyb; synaptic vesicle marker)
159 and found they were densely localized to γ1 compared to the other compartments,
160 complementary to the Brp compartmental heterogeneity of KCs (Figure 5A-5D). These
161 results suggest localized synaptic output of OANs along the γ lobe, potentially
162 underlying the Brp compartmental heterogeneity.
163 To examine the contribution of octopamine to the Brp accumulation within KCs,
164 we measured the Brp compartmental heterogeneity in the mutants of tyramine β-
165 hydroxylase (*Tβh*), the enzyme that catalyzes the synthesis of octopamine from
166 tyramine [46]. We generated two new *Tβh* null alleles: insertion mutant $T\beta h^{SK1\text{-}8}$ and
167 deletion mutant $T\beta h^{SK2\text{-}4}$ using CRISPR/Cas9-mediated mutagenesis. We visualized
168 Brp::rGFP in KCs of these mutants and found the significantly decreased
169 compartmental heterogeneity of the γ KCs (Figure 5E, Figure S6B). This suggests that
170 octopamine directly controls the AZ structure in KCs.
171 To identify the signaling pathway that regulates the Brp compartmental
172 heterogeneity, we knocked-down octopamine/tyramine receptors (including OAMB,
173 Octα2R, Octβ1R, Octβ2R, Octβ3R, OctTyrR, TyrR, TyrRII) in KCs using RNAi [43,47].
174 Among all the receptors tested, only Octβ2R knockdown significantly decreased the
175 compartmental heterogeneity (Figure 6A, Figure S6C-6D). We could not test the effect
176 of Octβ1R and Octβ3R because their deficiency in KCs caused abnormal development
177 of the MB. Octβ2R is coupled to the Gs alpha subunit to stimulate cyclic adenosine
178 monophosphate (cAMP) production [48]. To test whether cAMP plays a role in Brp
179 accumulation, we knocked-down the adenylate cyclase Rutabaga (Rut) in KCs using
180 RNAi [43,49–53]. The downregulation of Rut resulted in a significant decrease of the
181 compartmental heterogeneity (Figure 6B, Figure S6E), suggesting that octopamine
182 functions through Octβ2R-cAMP pathway.
183
184 **Nutritional states adjust the Brp compartmental heterogeneity through**
185 **octopamine signaling**
186 The spontaneous firing of octopamine neurons was shown to be decreased upon
187 starvation [54]. Therefore, we hypothesized state-dependent AZ remodeling through

188 octopamine (Figure 7A). To test this hypothesis, we starved the *Tβh* mutants for 48
189 hours and measured the Brp::rGFP heterogeneity in γ KCs. Indeed, there was no
190 significant state-dependent effect on the Brp compartmental heterogeneity in the *Tβh*
191 mutants (Figure 7B, Figure S6G). Taken together, we propose that internal states adjust
192 the synaptic output of MB compartments through octopamine signaling that supervise
193 the synaptic structures within KCs.
194
195 **DISCUSSION**
196 By labeling endogenous AZ scaffold protein Brp, we resolved individual AZs at
197 the single-cell level. The substantial intracellular heterogeneity of Brp accumulation
198 within γ KCs is found to be regulated by internal states of the animal. Other than the
199 compartmental heterogeneity of Brp clusters within KCs, our experimental pipeline
200 enables further profiling of other AZ characteristics such as the local AZ density [34].
201 How does octopaminergic signaling modify Brp accumulation? This study
202 identified the requirement of Octβ2R and Rut in regulating the AZ structure in KCs
203 (Figure 6). Octβ2R was shown to stimulate cAMP synthesis [48], suggesting that cAMP
204 could play a determining role. Consistent with this idea, *rut* mutant displays abnormal
205 AZ structures [55]. We propose that the localized innervations of octopamine neurons onto
206 KCs (Figure 5) results in different cAMP concentrations along the γ lobe. In both KCs
207 and motor neurons, cAMP concentration was shown to be locally regulated [56–58]. The
208 affinity or stability of Brp to AZs among different compartments is perhaps distinctly
209 set by the cAMP signaling compartmentation [59]. Interestingly, both DopR1 and Octβ2R
210 stimulate cAMP biosynthesis, while the knock-down of DopR1 had no significant effect
211 on the Brp heterogeneity (Figure 4). This may be due to different downstream targets of
212 the receptors including PKA [60].
213 AZ structures, especially Brp clusters, frequently serve as a proxy to explain
214 synaptic functions [5–7,15,17,40,61]. Consistent with previous studies, our data suggest that
215 Brp regulates the localization of Ca^{2+} channels in KCs [15,17,62]. Brp heterogeneity may
216 result in compartmental basal Ca^{2+} concentrations at AZs (Figure 3) and thus modulate
217 spontaneous synaptic vesicle release via the stochastic activity of Ca^{2+} channels [42].
218 Indeed, the enrichment of the Ca^{2+} channel is associated to higher spontaneous release
219 frequency in *Drosophila* NMJ [7,63] . Although the relationship between Brp
220 accumulation and evoked release in KCs seems more complicated since it involves
221 acute and compartmental dopaminergic modulations [13,64–66]. Unlike evoked activities,
222 spontaneous release of synaptic vesicle persists in the absence of stimulation thereby
223 affecting the states of the animal [10].
224 The Brp compartmental heterogeneity within KCs might directly modulate the
225 MB output through controlling the activity of different MBONs. Each type of MBONs
226 serves as an independent output unit, together regulating a variety of behaviors [11–
227 14,38,67–69]. Starvation changes the activity balance between MBON-γ1 and MBON-γ5
228 thus enhances appetitive memory expression [67,69,70], and MBON- γ5 and MBON- γ2
229 oppositely control sleep amount [71]. Consistently, we found that the compartmental AZ
230 heterogeneity within KCs, measured by Brp, decreased upon starvation (Figure 2E).
231 Considering the associations between octopamine and feeding behaviors [54,72–78], KCs
232 generates behavior adaptations in response to changing internal states and environments
233 by local AZ tuning [38,79,80].
234

SUPPLEMENTAL INFORMATION

Document S1. Figures S1-S6

ACKNOWLEDGEMENT

We thank all lab members of Tanimoto Lab at Tohoku University for valuable discussions. We thank Dr. Kate O'Connor-Giles (Brown University), Vienna Drosophila Resource Center (VDRC) and Bloomington Drosophila Stock Center (BDRC) for transgenic flies, Ayano Wu (Tohoku University) for graphical design. This study was supported by the Ministry of Education, Culture, Sports, Science and Technology (MEXT): 24H01217 (to H.T.), 22H04829 (to H.T.), 22H05481 (to H.T.), 22KK0106 (to H.T.), 20H00519 (to H.T.); Japan Science and Technology Agency (JST): JPMJSP2114 (to H.W.); Tohoku University Research Program 'Frontier Research in Duo' (to H.T.).

AUTHOR CONTRIBUTIONS

Conceptualization, H.W., N.Y. and H.T.; Investigation, H.W., S.E., K.S., A.A., K.J.; Methodology, H.W., N.Y., S.E. and Y.M.; Writing – Original Draft, H.W, S.E.; Writing – Review & Editing, H.W., S.E. and H.T.; Funding Acquisition, H.W. and H.T.; Resources, K.J. and S.K.; Supervision, D.W., N.Y., S.K. and H.T.

DECLARATION OF INTERESTS

The authors declare no competing interests.

MAIN FIGURE TITLES AND LEGENDS

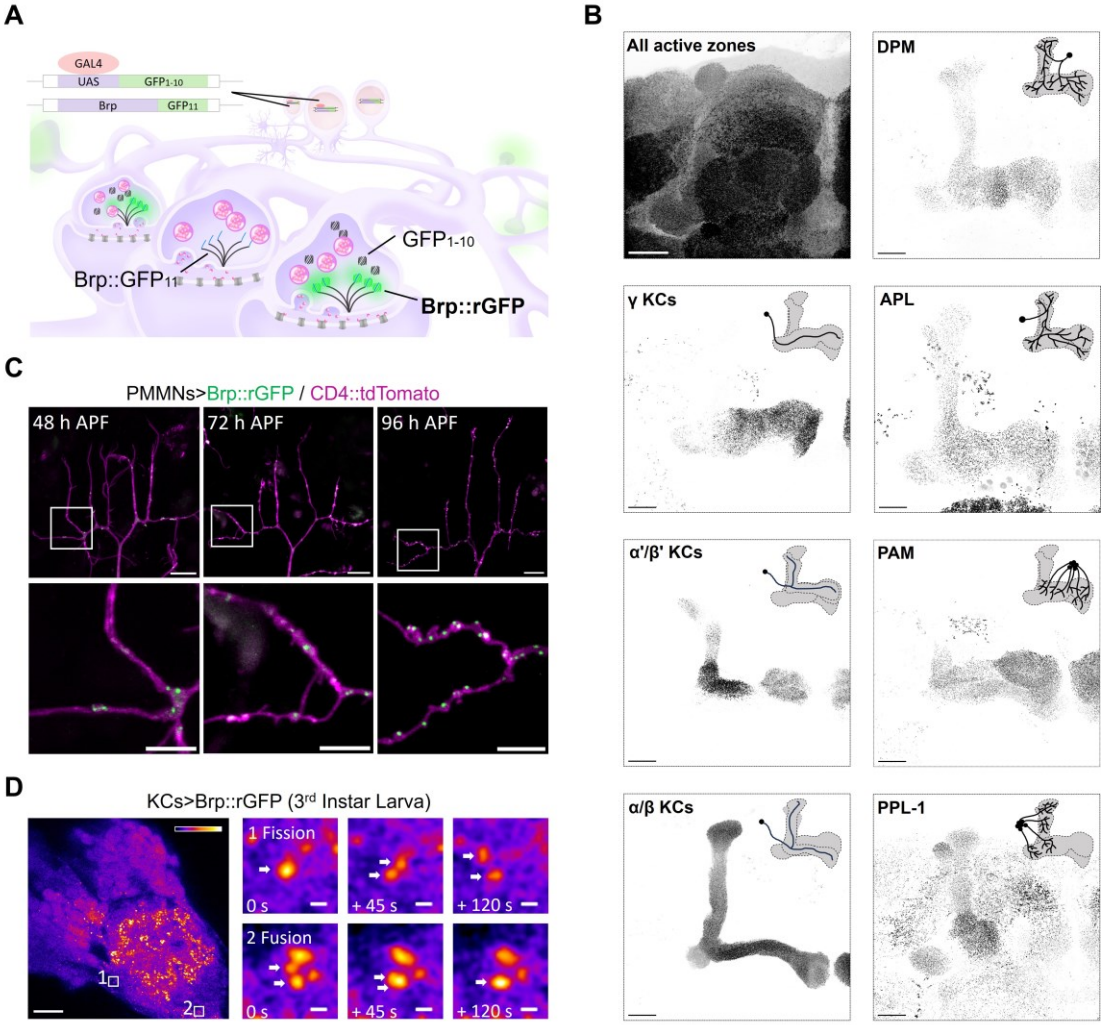

Figure 1. Cell-type specific dissection of the endogenous active zone scaffold

(A) Schematic of split-GFP tagging system. GFP_{11} was inserted prior to the stop codon of *brp*, while GFP_{1-10} was expressed in specific cell types using the GAL4-UAS system. GFP_{11} and GFP_{1-10} reconstitute to emit fluorescence.

(B) Visualization of Brp::rGFP in a cell-type specific manner. Immunostaining using antibody nc82 which labels all Brp in the brain, as a comparison to Brp::rGFP. Diagrams in each panel show the innervation pattern of neurons in the MB. GAL4 lines used: γ KCs (MB009B), α/β KCs (MB008B), α'/β' KCs (MB370B), PPL-1 (TH-GAL4), PAM (R58E02), DPM (VT64246), APL (GH146). Scale bar, 20 μm.

(C) Long-term live-imaging of Brp::rGFP (green) in a growing motor neuron (magenta, CD4::tdTomato) from 48 to 96 hours APF. OK371-GAL4 was used to express GFP_{1-10} and CD4::tdTomato. White boxes indicate zoomed-in areas shown in the lower panels. Scale bars: upper panels, 10 μm; lower panels, 5 μm.

(D) Ex vivo live-imaging of Brp::rGFP in 3rd instar larval KCs. GFP_{1-10} was expressed using R13F02-GAL4. The left panel shows the MB calyx region. White boxes indicate zoomed-in areas shown on the right panels. Box 1 and 2 demonstrate Brp::rGFP fission and fusion event. Whites arrows indicate Brp::rGFP clusters undergoing fission or fusion. Scale bars: left panel, 10 μm; right panels, 200 nm.

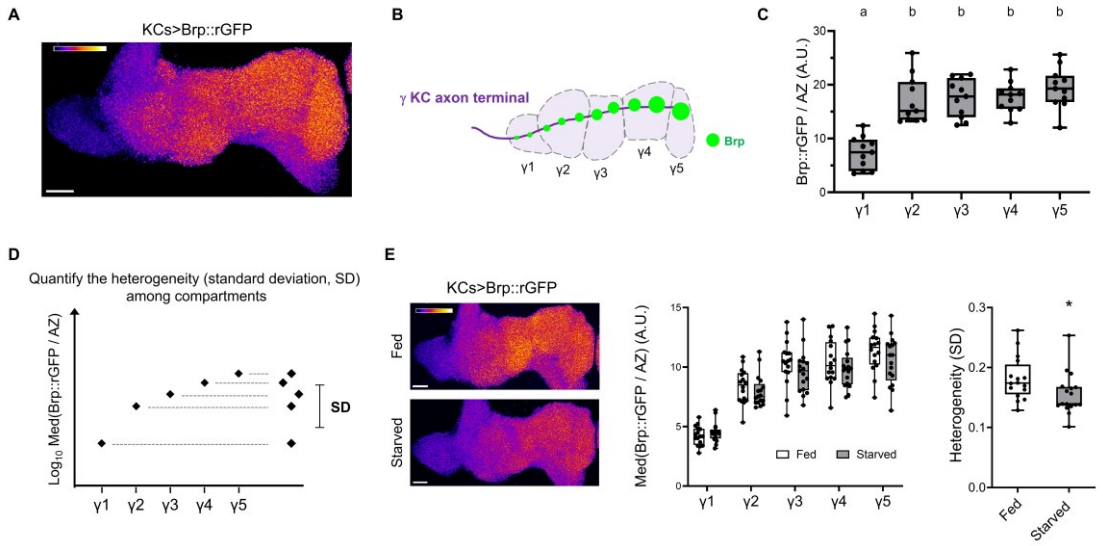

Figure 2. Compartmental presynaptic heterogeneity

(A) Brp::rGFP visualized in KCs. The horizontal lobe of the MB was imaged. Brp::rGFP was visualized using R13F02-GAL4.

(B) Diagram showing compartments in the MB γ lobe and the intracellular Brp localization in a single γ KC.

(C) Median intensity of Brp::rGFP clusters in each γ lobe compartment. Kruskal-Wallis test. n = 11. γ1 vs. γ2: P = 0.0012; γ1 vs. γ3: P = 0.0004; γ1 vs. γ4: P = 0.0004; γ1 vs. γ5: P < 0.0001.

(D) Standard deviation (SD) as an indicative of Brp::rGFP heterogeneity among compartments. Median Brp::rGFP intensity values of compartments were log-transformed for analysis. SD is calculated from five transformed medians.

(E) Starvation for 48 hours reduced The Brp compartmental heterogeneity in KCs. The middle panel shows the raw median Brp::rGFP intensities in each γ compartment for the control and starvation group. The heterogeneity (SD) was quantified for individual brain samples. Mann-Whitney U-test. Fed (n = 16) vs. Starved (n = 17): p = 0.0187; Scale bar, 10 μm.

Data are represented as box plots showing center (median), whiskers (Min. to Max.). Significant differences (P < 0.05) are indicated by distinct letters or *. Kruskal-Wallis test (C) and Mann-Whitney U-test (E).

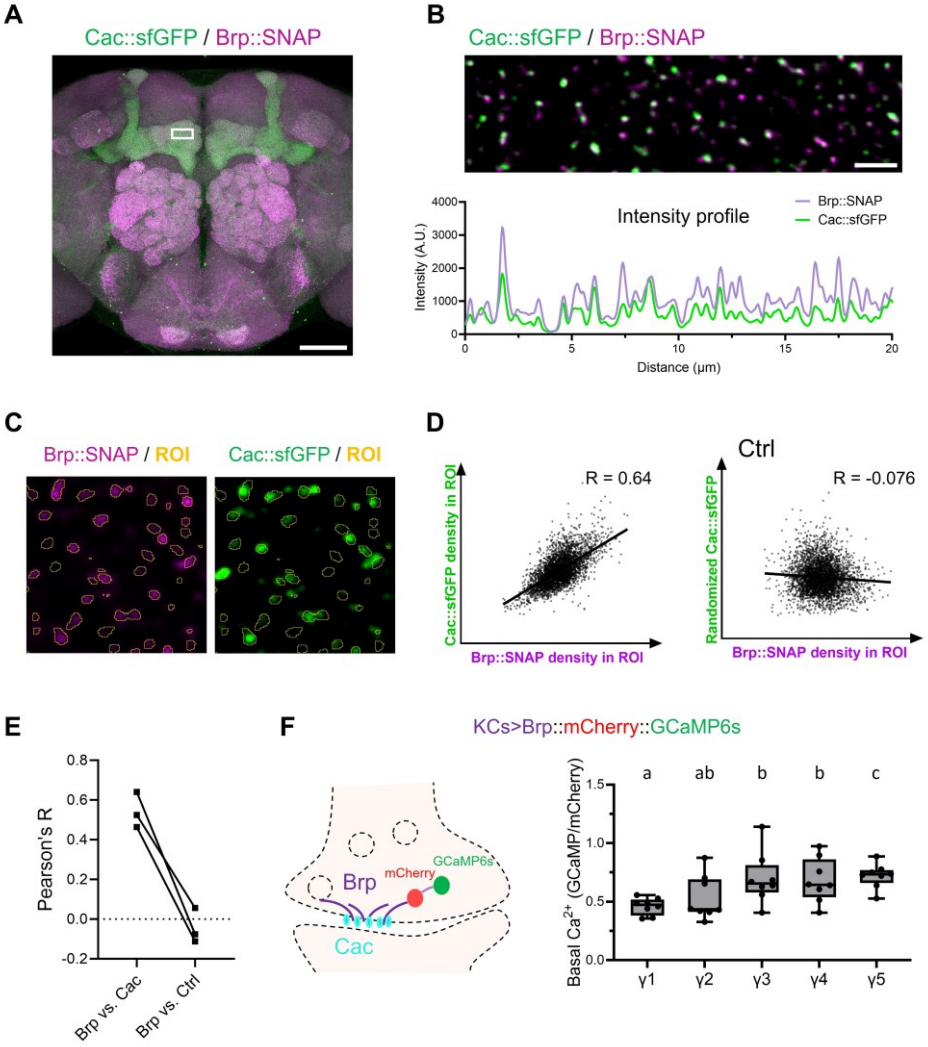

Figure 3. Brp is associated with Ca^{2+} channels in the fly brain

(A) Co-labeling of Cac::sfGFP (green) and Brp::SNAP (magenta) in an adult brain. The write box indicates the zoomed-in areas shown in (B**)**. Scale bar, 50 µm.

(B) Co-localization of Brp::SNAP and Cac::sfGFP signals. Signal intensity profiles of both Brp::SNAP (green) and Cac::sfGFP (magenta) in the image were plotted below. Scale bar, 10 µm.

(C) Correlation between Brp::SNAP (green) and Cac::sfGFP (magenta) signal intensities. The image is a selected area from γ5. Yellow circles show the 3D ROIs generated by segmenting Brp::SNAP signals. A loose setting was applied to include surrounding pixels. The same ROI set was used to quantify the signal density (total grey value divided by the ROI volume) for both Brp::SNAP and Cac::sfGFP.

(D) Scatter plot showing the correlation between Brp::SNAP and Cac::sfGFP signal intensities in an image sample. A 180˚ rotated Cac::sfGFP image was used as a control (see also Figure S4). Pearson's correlation coefficient (R) is shown.

(E) Pearson correlation coefficient (R) from three individual γ lobes showing the correlation between Brp::SNAP and Cac::sfGFP signal intensities.

(F) Basal Ca^{2+} concentration varies by compartment. The left panel shows the schematic of the Brp::mCherry::GCaMP6s ratio-matric sensor. GCaMP6s sensor is fused to

mCherry and Brp^{short}. The sensor was expressed by R13F02-GAL4 and GCaMP6s signal is normalized by mCherry for analysis. Kruskal-Wallis test. n = 8. γ1 vs. γ3: P = 0.0494; γ1 vs. γ4: P = 0.0494; γ1 vs. γ5: P = 0.0155; γ2 vs. γ5: P = 0.0494;
Data are represented as box plots showing center (median), whiskers (Min. to Max.).
Significant differences (P < 0.05) are indicated by distinct letters. Kruskal-Wallis test.

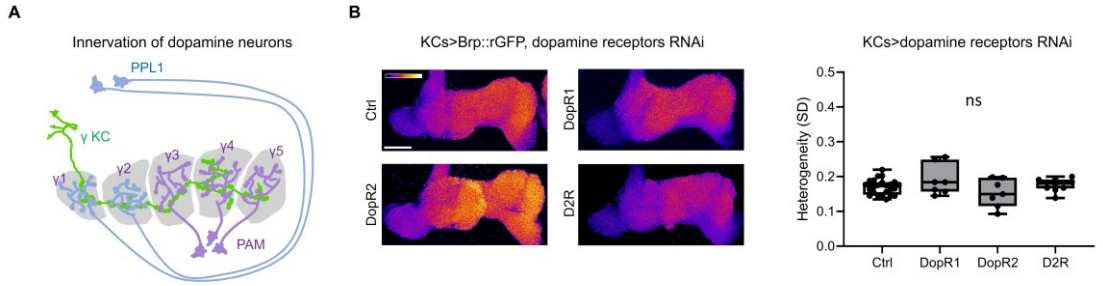

Figure 4. Dopamine receptors knockdown does not affect The Brp compartmental heterogeneity

(A) Schematic showing the innervation patterns of dopamine neurons. The γ lobe is innervated by dopamine neurons from the PPL1 and PAM clusters.
(B) Knockdown of dopamine receptors does not significantly alter the Brp compartmental heterogeneity. Three types of DA receptors, DopR1, DopR2 and D2R were knocked down using RNAi in KCs specifically with R13F02-GAL4. Representative images of Brp::rGFP from each group are shown. Scale bar: 20 μm. Ctrl (n = 24) vs. DopR1 (n = 7), DopR2 (n = 7) and D2R (n = 10): P > 0.05.
Data are represented as box plots showing center (median), whiskers (Min. to Max.). ns = not significant by Kruskal-Wallis test.

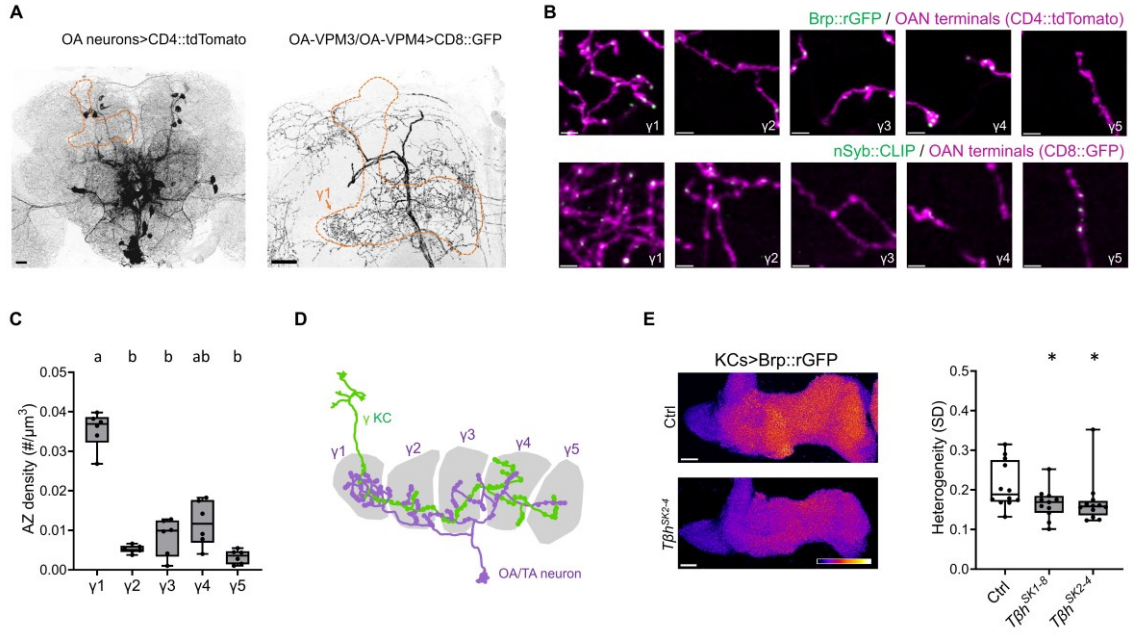

Figure 5. Octopamine controls the AZ structure in KCs

(A) OANs in the adult brain. OANs were labeled by Tdc2-GAL4 driven CD4::tdTomato in the left panel. OA-VPM3/4 neurons were labeled with MB022B-GAL4 [9] driven CD8::GFP (right panel). Dashed lines indicate the MB. Scale bars, 20

344 µm.
345 (B) AZ number and synaptic vesicle localization of OANs along the γ lobe. GFP_{1-10} and
346 CD4::tdTomato were expressed using Tdc2-GAL4. nSyb::CLIP labeling synaptic
347 vesicles and CD8::GFP were expressed using MB022B-GAL4. Scale bars, 2 µm.
348 Images were cropped from the same MB and are identical in size.
349 (C) AZ density of OANs across γ compartment. Brp::rGFP was visualized using Tdc2-
350 GAL4, and cluster density was quantified. n = 6 brains. Kruskal-Wallis test. γ1 vs. γ2: P
351 = 0.0066; γ1 vs. γ3: P =0.0319; γ1 vs. γ5: P =0.0004.
352 (D) Schematic showing the innervation pattern of OANs along the γ lobe.
353 (E) Reduced Brp compartmental heterogeneity in *Tβh* mutants. Representative images
354 of Brp::rGFP in control and $T\beta h^{SK2-4}$ background are shown. Scale bars, 10 µm.
355 Kruskal-Wallis test. Ctrl (n = 12) vs. $T\beta h^{SK1-8}$ (n = 11) and $T\beta h^{SK2-4}$ (n = 12). Ctrl vs.
356 $T\beta h^{SK1-8}$: P = 0.0442; Ctrl vs. $T\beta h^{SK2-4}$: P = 0.0228. *P < 0.05.
357 Data are represented as box plots showing center (median), whiskers (Min. to Max.).
358 Significant differences (P < 0.05) are indicated by distinct letters or *. Kruskal-Wallis
359 test.
360

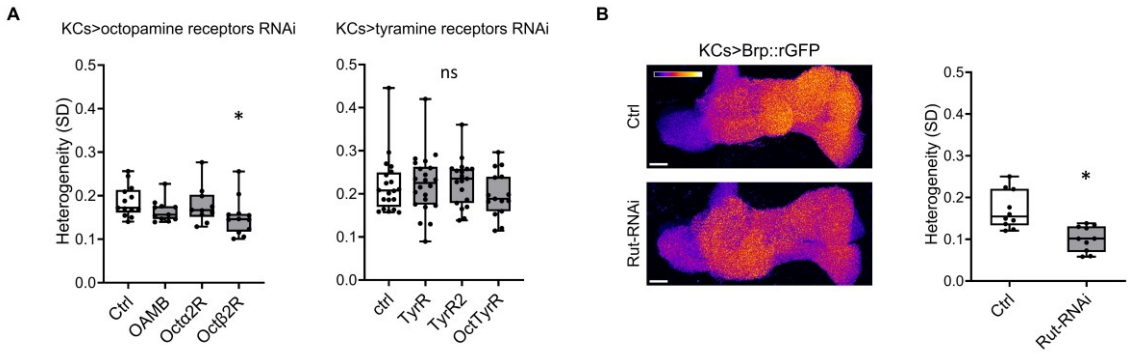

361
362 **Figure 6. Octβ2R and cAMP underly the Brp compartmental heterogeneity**
363 (A) Knockdown of Octβ2R reduced the Brp compartmental heterogeneity in γ KCs.
364 Receptors are knocked-down in γ KCs specifically using RNAi with R13F02-GAL4.
365 Kruskal-Wallis test. Ctrl (n = 13) vs. OAMB (n = 11), Octα2R (n = 10) and Octβ2R (n
366 = 12): P= 0.0228 for Ctrl vs. Octβ2R. Ctrl (n = 20) vs. TyrR (n = 22), TyrR2 (n = 22)
367 and OctTyrR (n = 15). *P < 0.05; ns = not significant.
368 (B) Knockdown of Rut significantly decreased the Brp compartmental heterogeneity in
369 γ KCs. Representative images showing Brp::rGFP in WT and in Rut knockdown group.
370 Mann-Whitney U-test. Ctrl (n = 10) vs. Rut-RNAi (n = 10): P = 0.0011.
371 Data are represented as box plots showing center (median), whiskers (Min. to Max.). *P
372 < 0.05 and ns = not significant. Kruskal-Wallis test (A) and Mann-Whitney U-test (B).
373

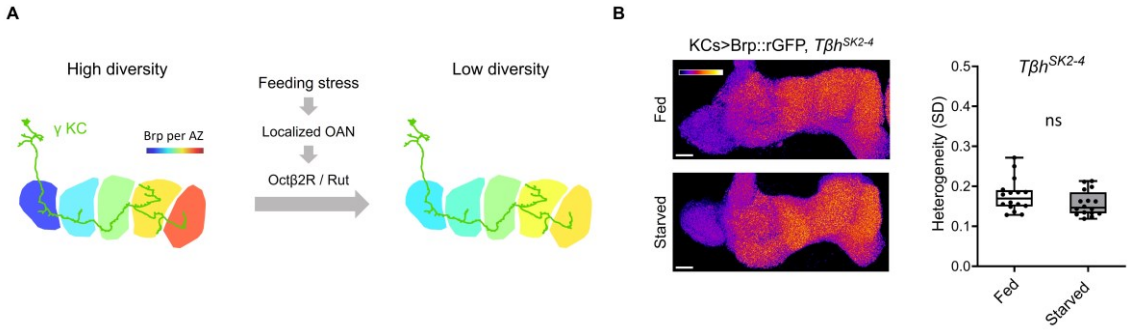

Figure 7. Nutritional states adjust the Brp compartmental heterogeneity through octopamine

(A) Graphical summary of the working model. Localized innervation of OANs onto γ KCs regulates the Brp accumulation and forms the Brp compartmental heterogeneity via Octβ2R and cAMP pathway. Nutritional states may modulate OAN activity, thereby adjusting the Brp heterogeneity.

(B) Starvation for 48 hours did not affect the Brp::rGFP compartmental heterogeneity in *Tβh*$^{SK2-4}$ mutant. GFP_{1-10} was expressed in KCs using R13F02-GAL4 in *Tβh*$^{SK2-4}$ background flies. Fed (n = 16) vs. starved (n = 17): $P > 0.05$.

Data are represented as box plots showing center (median), whiskers (Min. to Max.). ns = not significant by Mann-Whitney U-test.

387 **START★METHODS**

388

389 **KEY RESOURCE TABLE**

REAGENT or RESOURCE	SOURCE	IDENTIFIER
Antibodies		
Anti-Brp	DSHB	Cat#nc82; RRID: AB_2314866
AlexaFluor-568 goat anti-mouse	Invitrogen	Cat#A11004; RRID: AB_2534072
Chemicals, peptides, and recombinant proteins		
SNAP-Surface Alexa Fluor 647	New England Biolabs	Cat#S9136S
CLIP-Surface Alexa Fluor 647	New England Biolabs	Cat#S9234S
OMNIPAQUE 350	GE Healthcare	Cat#22000AMX02447
Histodenz	Sigma	Cat#D2158
Tetraspeck Microspheres 0.1 mm	Thermo Fisher Scientific	Cat#T7279
NaCl	Nacalai Tesque	Cat#31320-05
KCl	Nacalai Tesque	Cat#28514-75
TES	Nacalai Tesque	Cat#329810-55
Trehalose dihydrate	Tokyo Kasei Kogyo	Cat#T0331
D-glucose	Nacalai Tesque	Cat#16806-25
$NaHCO_3$	Nacalai Tesque	Cat#31213-15
NaH_2PO_4	Merck KGaA	Cat#106346
$CaCl_2$	Sigma-Aldrich	Cat#C5080
$MgCl_2$	Sigma-Aldrich	Cat#M2670
Experimental models: Organisms/strains		
Brp::SNAP	Bloomington Drosophila stock center (BDSC)	BDSC 58397
MB008B-GAL4	BDSC	BDSC 68291
MB009B-GAL4	BDSC	BDSC 68292
MB370B-GAL4	BDSC	BDSC 68319
VT64246-GAL4	VDRC	VDRC 204311
GH146-GAL4	BDSC	BDSC 30026
TH-GAL4	BDSC	BDSC 8848
R58E02-GAL4	BDSC	BDSC 41347
R13F02-GAL4	BDSC	BDSC 48571
OK371-GAL4	BDSC	BDSC 26160
UAS-Brp::mCherry::GCaMP6s	BDSC	BDSC 77131
Cac::sfGFP	Gratz et al. [6]	N/A
Tdc2-GAL4	BDSC	BDSC 9313
MB022B-GAL4	BDSC	BDSC 68298
UAS-nSyn::CLIP	BDSC	BDSC 58385
UAS-DopR1-RNAi	BDSC	BDSC 55239
UAS-Dop2R-RNAi	BDSC	BDSC 50621

UAS-DopR2-RNAi	BDSC	BDSC 51423
UAS-OAMB-RNAi	VDRC	VDRC 2861
UAS-Octα2R-RNAi	BDSC	BDSC 50678
UAS-Octβ1R-RNAi	BDSC	BDSC 58179
UAS-Octβ2R-RNAi	BDSC	BDSC 34673
UAS-Octβ3R-RNAi	BDSC	BDSC 62283
UAS-TyrR-RNAi	BDSC	BDSC 25857
UAS-TyrR2-RNAi	BDSC	BDSC 64964
UAS-OctTyrR-RNAi	BDSC	BDSC 28332
UAS-Rut-RNAi	BDSC	BDSC 80468
UAS-CD4::tdTomato	BDSC	BDSC 35841
UAS-CD8::GFP	BDSC	BDSC 32194
Tβh^{SK1-8}	This study	N/A
Tβh^{SK2-4}	This study	N/A
brp::GFP$_{11}$	This study	N/A
UAS-GFP$_{1-10}$	Kondo et al. [26]	N/A
Software and algorithms		
Python	N/A	N/A
Graphpad PRISM	Graphpad software	https://www.graphpad.com/
Fiji/Image J	NIH	https://imagej.net/software/fiji/downloads
Amira Software	Thermo Fisher Scientific	thermofisher.com/amira-avizo
DeconvolutionLab2	Sage et al. [81]	https://bigwww.epfl.ch/deconvolution/deconvolutionlab2/
CLIJ2	Haase et al. [82]	https://clij.github.io/
3D ImageJ Suite	Ollion et al. [83]	https://imagej.net/plugins/3d-imagej-suite/

RESOURCE AVAILBILITY

Lead contact

Further information and requests on resources and reagents should be directed to and will be fulfilled by the Lead Contact, Dr. Hiromu Tanimoto (hiromut@m.tohoku.ac.jp).

Material availability

All reagents generated in this study are available upon request from the Lead Contact.

Data and code availability

This study did not generate any unique code. All imaging data and quantification results reported in this paper are available from the Lead Contact upon request.

EXPERIMENTAL MODEL AND STUDY PARTICIPANT DETAILS

Animals

Flies were maintained on standard cornmeal food at 25 °C under a 12:12 hours light-

406 dark cycle for all experiments. All flies used for experiments are 3-7 days old adult
407 males. After hatching, adult flies were transferred to fresh food vials and flip every 2-3
408 days before experiments. In experiments where flies were fasted, the same population of
409 flies was separated before the experiment to ensure the homogeneity. All flies were
410 food-deprived for 48 hours for the experimental group, while provide normal food
411 supply for the control for the same time. The GAL4-UAS system was used to express
412 transgenes. For each transgenic control in RNAi experiments, crossing respective
413 transgenic line with Canton S strain, w1118, or y1w1118 to replace the balancer
414 chromosomes. Flies for wild-type characterization were also crossed to replace balancer
415 chromosomes. Strains used in this study are as indicated in the key resource table.
416
417 **METHOD DETAILS:**
418 **Transgenic lines and mutants**
419 Two independent null alleles of the *Tβh* gene were obtained by inducing frameshift
420 indels by the transgenic CRISPR/Cas9 system as previously described [84]. The following
421 20-bp gRNA sequences were used:
422 gRNA#1: GATACGTACACCAGTCCGGA
423 gRNA#2: GGTGAGACGGGACTACCAGC
424 $T\beta h^{SK1-8}$ was derived from mutagenesis by gRNA#1 and carries the following frameshift
425 insertion: CGTACACCAGgatggacactGGATGGACAG (the inserted sequence is
426 indicated by lower-case characters). $T\beta h^{SK2-4-4}$ was derived from mutagenesis by
427 gRNA#2 and carries the following frameshift deletion: TCCGGATGGA----------
428 ----------CTGTGAGGTC (the gap is indicated as hyphens). The *brp::GFP$_{11}$* line was
429 generated by targeted insertion of a GFP_{11} cassette into the endogenous *brp* locus just
430 prior to the stop codon as previously described [26].
431
432 **Sample preparation**
433 Animals used in experiments involving comparisons between control and experimental
434 groups were dissected on the same day. Data were collected from multiple batches of
435 experiments performed on different days. All steps were performed at room temperature
436 otherwise specified. Flies were anesthetized on ice and placed on ice before dissection.
437 The dissection was performed in ice PBS solution to collect the brain without the
438 ventral nerve cord. Brains are subsequently fixed by 2% paraformaldehyde for 1 hour
439 then washed 3×20 min with 0.1% PBT (0.1% Triton X-100 in PBS) in a PCR tube,
440 typically containing 5-6 brains.
441 For SNAP or CLIP chemical tagging, brains were incubated in SNAP-Surface
442 647 (1:1000; NEB; S9136S) or CLIP-Surface 647 (1:1000; NEB; S9234S) in 0.3% PBT
443 for 15 min and washed with 3×20 min with 0.1% PBT. Samples are mounted on
444 microscope slides using the appropriate mounting medium (SeeDB2S, SeeDB2G [85] or
445 86% glycerol according to the imaging condition). Brp::SNAP, Brp::rGFP, Cac::sfGFP,
446 CD4::tdTomato and CD8::GFP samples were imaged without immunohistochemistry.
447 Immunohistochemistry procedures (for anti-Brp staining in Figure 1B) were
448 carried out as described [86]. In brief, fixed brains were washed 3×20 min with 0.1% PBT
449 and incubated in 3% normal goat serum (NGS; Sigma-Aldrich; G9023) for 1 hour at
450 room temperature. Antibodies used were as indicated in key resource table. Brains were
451 incubated in antibody solutions at 4°C for 48 hours for both primary and secondary
452 antibodies. Sub-resolution fluorescent beads (Tetraspeck Microspheres 0.1 mm, Thermo

453 Fisher Scientific, T7279) were imaged for generating experimental point spread
454 function (PSF). The beads solution was diluted with distilled water and sonicated
455 multiple times to eliminate aggregation.
456 For *in vivo* imaging of PM-Mns in developing pupae, samples were prepared as
457 previously described [30]. In brief, white prepupal stage pupae (~ 0 hour APF) were
458 collected and incubated at 25 °C until the experiment. Before imaging, the puparium
459 case was carefully removed with forceps, and the pupa was transferred to an imaging
460 chamber sealed with a cover slip to create an imaging window on the abdomen. For ex
461 vivo imaging of 3rd instar pupal CNS, the CNS was dissected directly from the animal
462 in PBS at room temperature. The CNS sample was then mounted with a spacer between
463 the microscopic glass and cover slip with PBS, The entire process, from dissection to
464 imaging, was performed within 5 minutes.
465
466 **Image acquisition**
467 For fixed samples and *ex vivo* imaging, images are acquired using the Olympus FV1200
468 confocal microscope platform equipped with GaAsP high sensitivity detectors and a
469 60×/1.42 NA oil immersion objective (PLAPON60XO, Olympus) and a 30×/1.05 NA
470 silicone immersion objective (UPLSAPO30XS, Olympus). For *in vivo* imaging on
471 pupae, images were acquired using the Zeiss LSM 800 series confocal microscopy
472 equipped with a 40×/1.3 NA objective (Plan-Apochromat 40×/1.3 Oil DIC (UV) VIS-IR
473 M27).
474 For Brp::SNAP chemical tagging, 30×/1.05 NA objective is used with a voxel
475 size of 0.53 µm × 0.53 µm × 0.84 µm (lateral × lateral × axial) to image the whole brain
476 except for the optical lobes. For Brp::rGFP and UAS-CD4::tdTomato samples in all
477 GAL4 types except Tdc2-GAL4, 60×/1.42 NA oil immersion objective was used and
478 473 nm laser power: 0.1%; 559 nm laser power: 0.1%; scanning speed: 2 µs/pixel with a
479 voxel size of lateral 0.079 × 0.079 × axial 0.370 µm. For Brp::SNAP/Cac::sfGFP
480 images, 60×/1.42 NA objective is used with a voxel size of 0.079 × 0.079 × 0.370 µm.
481 For Tdc2-GAL4 driven UAS4-CD8::GFP and UAS-nSyb::CLIP samples, 30×/1.05 NA
482 objective is used with a voxel size of 0.414 × 0.414 × 0.84 µm. For MB022B-GAL
483 driven UAS-CD8::GFP and UAS-nSyb-CLIP samples, 30×/1.05 NA objective is used
484 with a voxel size of 0.276 × 0.276 × 0.87 µm. For Tdc2-GAL4 driven Brp::rGFP and
485 UAS-CD4::tdTomato, 60×/1.42 NA objective is used with a scanning voxel size of
486 0.132 × 0.132 × 0.34 µm. For Brp::rGFP *in vivo* imaging of PM-Mns, a 40×/1.3 NA
487 objective is used with a voxel size of 0.0725 × 0.0725 × 0.460 µm. For Brp::rGFP ex
488 vivo imaging, 60×/1.42 NA objective is used with a voxel size of 0.079 × 0.079 × 0.370
489 µm and 473 nm laser power: 2.0%. For experimental PSF imaging, SeeDB2S immerged
490 beads were scanned in a setting that is 60×/1.42 NA oil immersion objective; 473 nm
491 laser power: 2.0%; 559 nm laser power: 1.5%; voxel size: 0.079 µm × 0.079 µm ×
492 0.370 µm; scanning speed: 4 µs/pixel, to produce multiple bead images.
493
494 ***In vivo* calcium imaging**
495 *In vivo* calcium imaging was performed following a previously described protocol [86].
496 Briefly, flies were anesthetized on ice for 3 minutes and placed in a custom-made
497 holding dish on a Peltier plate (CP-085, Sinics) maintained at 5°C. The head capsule
498 was fixed to the dish using UV curing optical adhesive (NOA68, Thorlabs). To
499 minimize brain movement, the proboscis was glued to the capsule A small window was

500 opened on the top of the head capsule, and the exposed area was filled with *Drosophila*
501 saline solution (final concentration: 103 mM NaCl, 3 mM KCl, 5 mM TES, 8 mM
502 Trehalose dihydrate, 10 mM D-glucose, 26 mM $NaHCO_3$, 1 mM NaH_2PO_4, 1.5 mM
503 $CaCl_2$, 4 mM $MgCl_2$, adjust to pH ~7.2). Air sacs and fat bodies covering the brain
504 surface were carefully removed. Live imaging was conducted using a laser scanning
505 confocal microscope equipped with GaAsP detectors (A1R, Nikon) and a 30×/1.1 NA
506 water immersion objective (Apo LWD 25×, Nikon). GCaMP6s and mCherry were
507 sequentially excited at 488 and 561 nm, respectively. Emission light was collected using
508 dichroic mirrors and emission filters (BP500–550 and BP570-620) onto GaAsP
509 detectors. The MB γ lobe was scanned at a pixel size of 0.5μm/pixel (512 × 128 pixels)
510 at a frame rate of 1 Hz using line scans with 16× averages in the resonant scanning
511 mode. The pinhole was set to 2.5 AU (561 nm). For recording, images were
512 sequentially acquired over 40 s and saved for later image processing.
513
514 **QUANTIFICATION AND STAISTICAL ANALYSIS**
515 **Data processing and analysis**
516 PSF images were processed in the Amira software (Thermo Fisher Scientific). Using the
517 Extract Point Spread Function module, PSFs extracted from each image were averaged
518 into a single PSF, which was later used for image deconvolution (resized voxel size:
519 0.079 μm × 0.079 μm × 0.370 μm; image size: 32 pixels × 32 pixels × 21 slices). Image
520 deconvolution was performed using the Richardson-Lucy iterative non-blind algorithm
521 in the Fiji plugin DeconvolutionLab2 [81], or with CLIJ2 GPU-based Richardson-Lucy
522 deconvolution [82].
523 AZ detection was performed as described [34] in a compartmental manner. In
524 brief, a sub-image stacks were cropped from every MB compartment in the original
525 image. Compartments were manually identified referencing the CD4::tdTomato
526 membrane signal. An intensity threshold was applied to reduce background noise. Sub-
527 stacks were processed by the 3D maxima finder and the 3D spot segmentation function
528 in the 3D suite plugin [83] in Fiji. 3D maxima were detected for each cluster and used as
529 start points for pixel clustering using the 3D spot segmentation function. This process
530 created 3D ROIs enclosing individual Brp clusters. ROIs were then used to extract
531 signal intensities and cluster coordinates. Detection precision was optimized by
532 comparing detection results with manually defined ground truths as previously
533 described.
534 For calcium imaging, ROIs were manually drawn for each compartment in time-
535 series image stacks. GCaMP6s signal was normalized by mCherry in each time-frame
536 using the image calculator in Fiji. The mean intensity was calculated in each
537 compartment by averaging 7 frames without any odor stimulation as the basal level.
538
539 **Statistical analysis**
540 Statistical analyses were performed using GraphPad Prism version 8, 9 and 10.
541 Summarized data are represented as box plots showing center (median), whiskers (Min.
542 to Max.). For comparison between more than two groups, Kruskal-Wallis test with
543 original False Discovery Rate (FDR) method of Benjamini and Hochberg correction
544 was applied. Desired false discovery rate was set to 0.05. For comparison between two
545 groups, unpaired nonparametric two-sided Mann-Whitney U-test was used. Pearson's
546 correlation coefficient (R) was calculated in Python.

SUPPLEMENTAL FIGURE TITLES AND LEGENDS

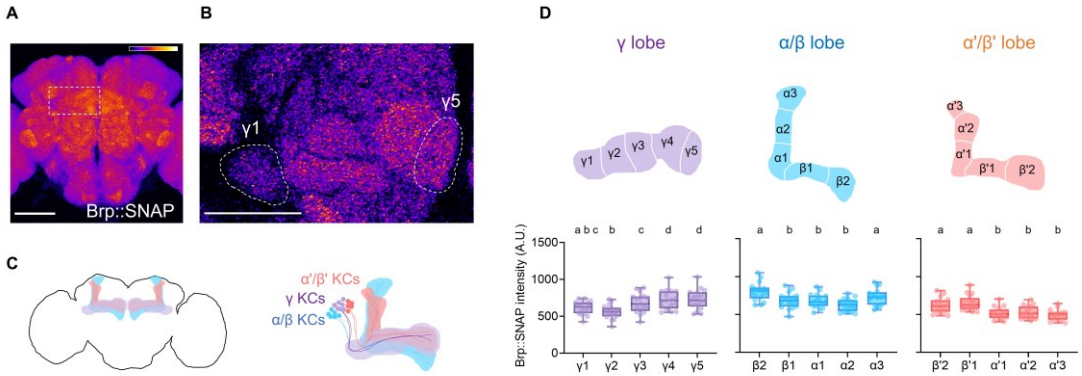

Figure S1. Heterogeneous Brp enrichment in the MB

(A) SNAP chemical tagging labeled endogenous Brp in the brain. Scale bar, 100 µm. The dash line area in indicates the zoomed-in area showed in (B).

(B) Intensity difference of Brp::SNAP between γ1 and γ5 compartment on the same imaging plate. Scale bar, 50 µm.

(C) Schematic of the MB. The MB comprise three lobes based on the projection patterns of three KC subtypes: γ KCs, α'/β' KCs and α/β KCs.

(D) Brp::SNAP intensity difference across compartments. Schematic drawings above indicate compartments of each lobe.

Data are represented as box plots showing center (median), whiskers (Min. to Max.). Significant differences ($P < 0.05$) are indicated by distinct letters. Kruskal-Wallis test.

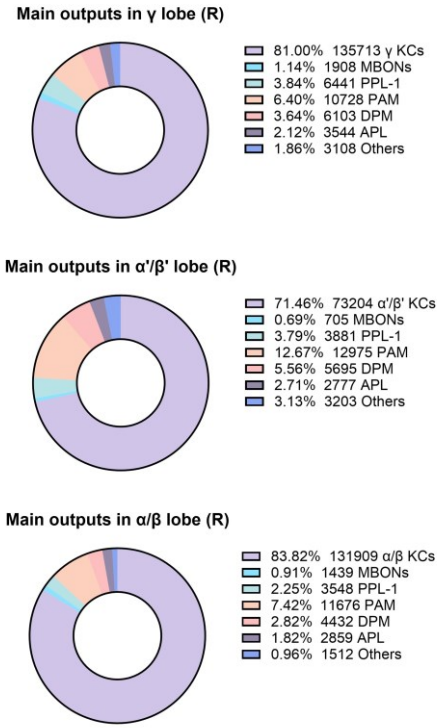

Figure S2. Pre-synapses in the MB are predominantly from KCs.

Pie charts showing the composition of pre-synapses in each of the three MB lobes. Data is from the hemibrain online data but not all the cell types are listed. The number of pre-synapse and the percentage are indicated for each cell type, including KCs, MBONs PPL-1 neurons, PAM neurons, dorsal paired medial (DPM) neuron and anterior paired lateral (APL) neuron.

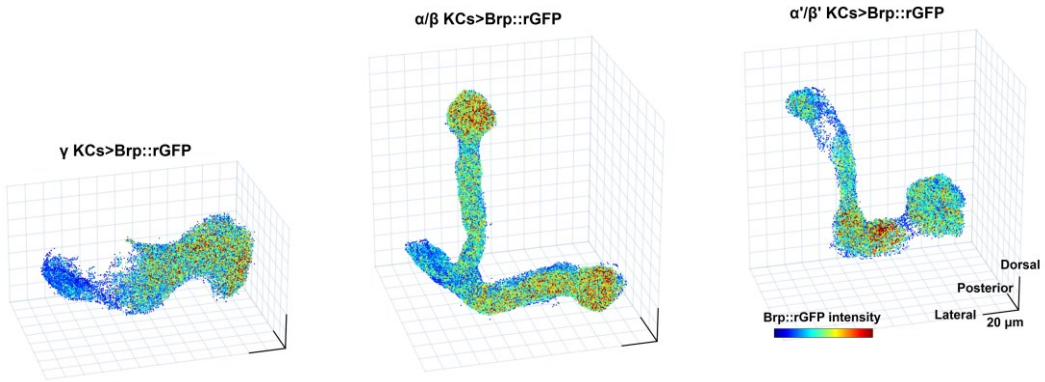

Figure S3. Brp compartmental heterogeneity in different KC subtypes
The 3D reconstruction of Brp::rGFP clusters, colored by Brp::rGFP intensity. Brp::rGFP is visualized in γ KCs using MB009B-GAL4, in α/β KCs using MB008B-GAL4 and in α'/β' KCs using MB0370B-GAL4. Scale bars, 20 µm.

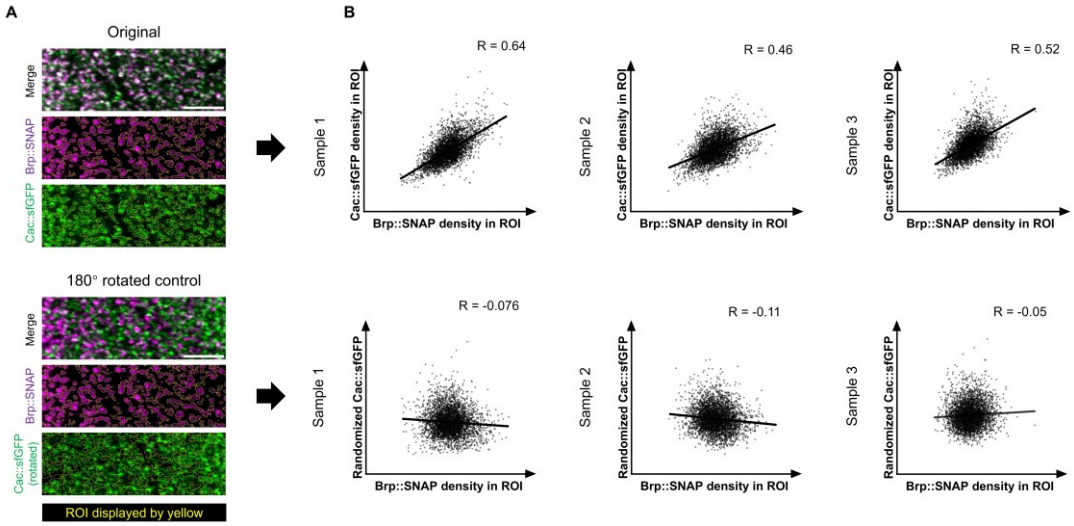

Figure S4. Correlation between Brp::SNAP and Cac::sfGFP signals intensities
(A) Correlation analysis of Brp::SNAP and Cac::sfGFP signal intensities. ROIs are generated using 3D spot segmentation method without a watershed process. Relatively loose setting was applied on Brp::SNAP images to generate wide ROIs. The same ROI set was used to calculated signal intensities in both Brp::SNAP and Cac::sfGFP channels. The 180˚ rotated version of Cac::sfGFP image was used as the control. A total of 4000 ROIs were analyzed, and Pearson correlation coefficient (R) values were calculated for each sample. Scale bars, 5 µm.
(B) Scatter plots showing the correlation between Brp::SNAP and Cac::sfGFP signal intensities (left) and control (right) in different brain samples. R value is indicated for each sample.

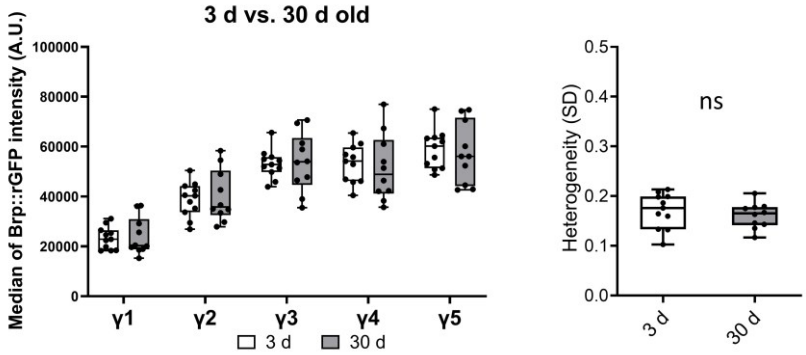

Figure S5. Brp compartmental heterogeneity in aging flies
Median intensity of Brp::rGFP clusters and the Brp::rGFP compartmental heterogeneity were compared between 3 days old and 30 days old flies. Mann-Whitney U-test, 3 d (n = 11) vs. 30 d (n = 10): $p > 0.05$.
Data are represented as box plots showing center (median), whiskers (Min. to Max.). ns = not significant by Mann-Whitney U-test.

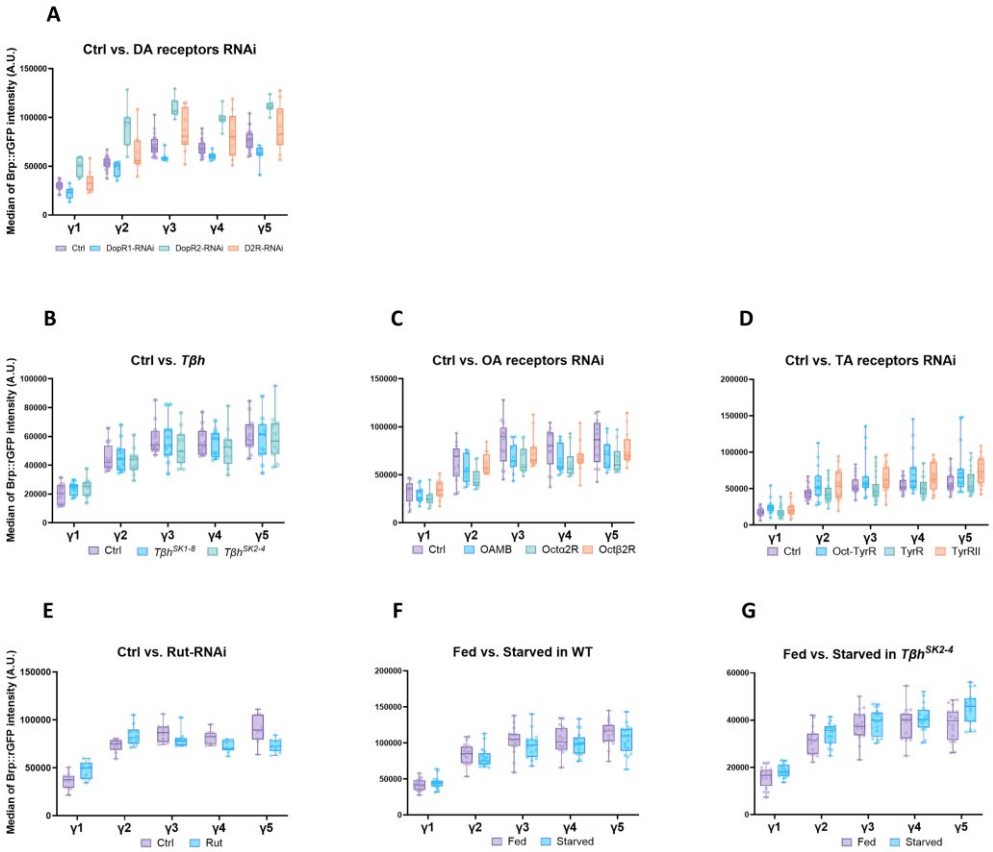

Figure S6. Median intensities of Brp::rGFP clusters in each experiment
(A) Dopamine receptor knockdown experiment.
(B) *Tβh* mutant's experiment.
(C) Octopamine receptor knockdown experiment.
(D) Tyramine receptor knockdown experiment.

603 (E) Rut knockdown experiment.
604 (F) Starvation experiment.
605 (G) Starvation experiment of $T\beta h^{SK2\text{-}4}$ mutants.
606 Data are represented as box plots showing center (median), whiskers (Min. to Max.).

607 **REFERENCES**
608

609 1. O'Rourke, N.A., Weiler, N.C., Micheva, K.D., and Smith, S.J. (2012). Deep
610 molecular diversity of mammalian synapses: why it matters and how to measure it. Nat
611 Rev Neurosci *13*, 365–379. https://doi.org/10.1038/nrn3170.

612 2. Cizeron, M., Qiu, Z., Koniaris, B., Gokhale, R., Komiyama, N.H., Fransén, E., and
613 Grant, S.G.N. (2020). A brainwide atlas of synapses across the mouse life span. Science
614 *369*, 270–275. https://doi.org/10.1126/science.aba3163.

615 3. Ehmann, N., Linde, S. van de, Alon, A., Ljaschenko, D., Keung, X.Z., Holm, T.,
616 Rings, A., DiAntonio, A., Hallermann, S., Ashery, U., et al. (2014). Quantitative super-
617 resolution imaging of Bruchpilot distinguishes active zone states. Nat Commun *5*, 4650.
618 https://doi.org/10.1038/ncomms5650.

619 4. Paul, M.M., Pauli, M., Ehmann, N., Hallermann, S., Sauer, M., Kittel, R.J., and
620 Heckmann, M. (2015). Bruchpilot and Synaptotagmin collaborate to drive rapid
621 glutamate release and active zone differentiation. Front Cell Neurosci *9*, 29.
622 https://doi.org/10.3389/fncel.2015.00029.

623 5. Akbergenova, Y., Cunningham, K.L., Zhang, Y.V., Weiss, S., and Littleton, J.T.
624 (2018). Characterization of developmental and molecular factors underlying release
625 heterogeneity at Drosophila synapses. Elife *7*, e38268.
626 https://doi.org/10.7554/elife.38268.

627 6. Gratz, S.J., Goel, P., Bruckner, J.J., Hernandez, R.X., Khateeb, K., Macleod, G.T.,
628 Dickman, D., and O'Connor-Giles, K.M. (2019). Endogenous tagging reveals
629 differential regulation of Ca2+ channels at single AZs during presynaptic homeostatic
630 potentiation and depression. J Neurosci *39*, 3068–18.
631 https://doi.org/10.1523/jneurosci.3068-18.2019.

632 7. Newman, Z.L., Bakshinskaya, D., Schultz, R., Kenny, S.J., Moon, S., Aghi, K.,
633 Stanley, C., Marnani, N., Li, R., Bleier, J., et al. (2022). Determinants of synapse
634 diversity revealed by super-resolution quantal transmission and active zone imaging.
635 Nat Commun *13*, 229. https://doi.org/10.1038/s41467-021-27815-2.

636 8. Tanaka, N.K., Tanimoto, H., and Ito, K. (2008). Neuronal assemblies of the
637 Drosophila mushroom body. J. Comp. Neurol. *508*, 711–755.
638 https://doi.org/10.1002/cne.21692.

639 9. Aso, Y., Hattori, D., Yu, Y., Johnston, R.M., Iyer, N.A., Ngo, T.-T., Dionne, H.,
640 Abbott, L., Axel, R., Tanimoto, H., et al. (2014). The neuronal architecture of the
641 mushroom body provides a logic for associative learning. Elife *3*, e04577.
642 https://doi.org/10.7554/elife.04577.

643 10. Suárez-Grimalt, R., Kadow, I.C.G., and Scheunemann, L. (2024). An integrative
644 sensor of body states: how the mushroom body modulates behavior depending on
645 physiological context. Learn. Mem. *31*, a053918.
646 https://doi.org/10.1101/lm.053918.124.

647 11. Aso, Y., Sitaraman, D., Ichinose, T., Kaun, K.R., Vogt, K., Belliart-Guérin, G.,
648 Plaçais, P.-Y., Robie, A.A., Yamagata, N., Schnaitmann, C., et al. (2014). Mushroom
649 body output neurons encode valence and guide memory-based action selection in
650 Drosophila. eLife *3*, e04580. https://doi.org/10.7554/elife.04580.

651 12. Ichinose, T., Kanno, M., Wu, H., Yamagata, N., Sun, H., Abe, A., and Tanimoto, H.
652 (2021). Mushroom body output differentiates memory processes and distinct memory-
653 guided behaviors. Curr Biol *31*, 1294-1302.e4.
654 https://doi.org/10.1016/j.cub.2020.12.032.

655 13. Cohn, R., Morantte, I., and Ruta, V. (2015). Coordinated and Compartmentalized
656 Neuromodulation Shapes Sensory Processing in Drosophila. Cell *163*, 1742–1755.
657 https://doi.org/10.1016/j.cell.2015.11.019.

658 14. Owald, D., Felsenberg, J., Talbot, C.B., Das, G., Perisse, E., Huetteroth, W., and
659 Waddell, S. (2015). Activity of Defined Mushroom Body Output Neurons Underlies
660 Learned Olfactory Behavior in Drosophila. Neuron *86*, 417–427.
661 https://doi.org/10.1016/j.neuron.2015.03.025.

662 15. Kittel, R.J., Wichmann, C., Rasse, T.M., Fouquet, W., Schmidt, M., Schmid, A.,
663 Wagh, D.A., Pawlu, C., Kellner, R.R., Willig, K.I., et al. (2006). Bruchpilot Promotes
664 Active Zone Assembly, Ca^{2+} Channel Clustering, and Vesicle Release. Science *312*,
665 1051–1054. https://doi.org/10.1126/science.1126308.

666 16. Wagh, D.A., Rasse, T.M., Asan, E., Hofbauer, A., Schwenkert, I., Dürrbeck, H.,
667 Buchner, S., Dabauvalle, M.-C., Schmidt, M., Qin, G., et al. (2006). Bruchpilot, a
668 Protein with Homology to ELKS/CAST, Is Required for Structural Integrity and
669 Function of Synaptic Active Zones in Drosophila. Neuron *49*, 833–844.
670 https://doi.org/10.1016/j.neuron.2006.02.008.

671 17. Fouquet, W., Owald, D., Wichmann, C., Mertel, S., Depner, H., Dyba, M.,
672 Hallermann, S., Kittel, R.J., Eimer, S., and Sigrist, S.J. (2009). Maturation of active
673 zone assembly by Drosophila Bruchpilot. J Cell Biol *186*, 129–145.
674 https://doi.org/10.1083/jcb.200812150.

675 18. Matkovic, T., Siebert, M., Knoche, E., Depner, H., Mertel, S., Owald, D., Schmidt,
676 M., Thomas, U., Sickmann, A., Kamin, D., et al. (2013). The Bruchpilot cytomatrix
677 determines the size of the readily releasable pool of synaptic vesicles. J Cell Biol *202*,
678 667–683. https://doi.org/10.1083/jcb.201301072.

679 19. Takemura, S., Aso, Y., Hige, T., Wong, A., Lu, Z., Xu, C.S., Rivlin, P.K., Hess, H.,
680 Zhao, T., Parag, T., et al. (2017). A connectome of a learning and memory center in the
681 adult Drosophila brain. Elife *6*, e26975. https://doi.org/10.7554/elife.26975.

682 20. Li, F., Lindsey, J.W., Marin, E.C., Otto, N., Dreher, M., Dempsey, G., Stark, I.,
683 Bates, A.S., Pleijzier, M.W., Schlegel, P., et al. (2020). The connectome of the adult
684 Drosophila mushroom body provides insights into function. eLife *9*, e62576.
685 https://doi.org/10.7554/elife.62576.

686 21. Chu, L.-A., Lu, C.-H., Yang, S.-M., Liu, Y.-T., Feng, K.-L., Tsai, Y.-C., Chang, W.-
687 K., Wang, W.-C., Chang, S.-W., Chen, P., et al. (2019). Rapid single-wavelength
688 lightsheet localization microscopy for clarified tissue. Nat Commun *10*, 4762.
689 https://doi.org/10.1038/s41467-019-12715-3.

690 22. Gao, R., Asano, S.M., Upadhyayula, S., Pisarev, I., Milkie, D.E., Liu, T.-L., Singh,
691 V., Graves, A., Huynh, G.H., Zhao, Y., et al. (2019). Cortical column and whole-brain
692 imaging with molecular contrast and nanoscale resolution. Science *363*.
693 https://doi.org/10.1126/science.aau8302.

694 23. Chen, Y., Akin, O., Nern, A., Tsui, C.Y.K., Pecot, M.Y., and Zipursky, S.L. (2014).
695 Cell-type-Specific Labeling of Synapses In Vivo through Synaptic Tagging with
696 Recombination. Neuron *81*, 280–293. https://doi.org/10.1016/j.neuron.2013.12.021.

697 24. Gärtig, P.-A., Ostrovsky, A., Manhart, L., Giachello, C.N.G., Kovacevic, T., Lustig,
698 H., Chwalla, B., Cachero, S., Baines, R.A., Landgraf, M., et al. (2019). Motor circuit
699 function is stabilized during postembryonic growth by anterograde trans-synaptic Jelly
700 Belly - Anaplastic Lymphoma Kinase signaling. bioRxiv, 841106.
701 https://doi.org/10.1101/841106.

702 25. Kamiyama, D., Sekine, S., Barsi-Rhyne, B., Hu, J., Chen, B., Gilbert, L.A.,
703 Ishikawa, H., Leonetti, M.D., Marshall, W.F., Weissman, J.S., et al. (2016). Versatile
704 protein tagging in cells with split fluorescent protein. Nat. Commun. *7*, 11046.
705 https://doi.org/10.1038/ncomms11046.

706 26. Kondo, S., Takahashi, T., Yamagata, N., Imanishi, Y., Katow, H., Hiramatsu, S.,
707 Lynn, K., Abe, A., Kumaraswamy, A., and Tanimoto, H. (2020). Neurochemical
708 Organization of the Drosophila Brain Visualized by Endogenously Tagged
709 Neurotransmitter Receptors. Cell Reports *30*, 284-297.e5.
710 https://doi.org/10.1016/j.celrep.2019.12.018.

711 27. Kohl, J., Ng, J., Cachero, S., Ciabatti, E., Dolan, M.-J., Sutcliffe, B., Tozer, A.,
712 Ruehle, S., Krueger, D., Frechter, S., et al. (2014). Ultrafast tissue staining with
713 chemical tags. Proc. Natl. Acad. Sci. *111*, E3805–E3814.
714 https://doi.org/10.1073/pnas.1411087111.

715 28. Jenett, A., Rubin, G.M., Ngo, T.-T.B., Shepherd, D., Murphy, C., Dionne, H.,
716 Pfeiffer, B.D., Cavallaro, A., Hall, D., Jeter, J., et al. (2012). A GAL4-Driver Line

717 Resource for Drosophila Neurobiology. Cell Rep. *2*, 991–1001.
718 https://doi.org/10.1016/j.celrep.2012.09.011.

719 29. Waddell, S., Armstrong, J.D., Kitamoto, T., Kaiser, K., and Quinn, W.G. (2000).
720 The amnesiac Gene Product Is Expressed in Two Neurons in the Drosophila Brain that
721 Are Critical for Memory. Cell *103*, 805–813. https://doi.org/10.1016/s0092-
722 8674(00)00183-5.

723 30. Constance, W.D., Mukherjee, A., Fisher, Y.E., Pop, S., Blanc, E., Toyama, Y., and
724 Williams, D.W. (2018). Neurexin and Neuroligin-based adhesion complexes drive
725 axonal arborisation growth independent of synaptic activity. Elife *7*, e31659.
726 https://doi.org/10.7554/elife.31659.

727 31. McDonald, N.A., Fetter, R.D., and Shen, K. (2020). Assembly of synaptic active
728 zones requires phase separation of scaffold molecules. Nature *588*, 454–458.
729 https://doi.org/10.1038/s41586-020-2942-0.

730 32. Lucy, L.B. (1974). An iterative technique for the rectification of observed
731 distributions. Astronomical J *79*, 745. https://doi.org/10.1086/111605.

732 33. Richardson, W.H. (1972). Bayesian-Based Iterative Method of Image Restoration*.
733 J Opt Soc Am *62*, 55. https://doi.org/10.1364/josa.62.000055.

734 34. Wu, H., Maekawa, Y., Eno, S., Kondo, S., Yamagata, N., and Tanimoto, H. (2024).
735 Synapse profiling of identified neurons in the Drosophila brain. bioRxiv,
736 2024.12.02.626511. https://doi.org/10.1101/2024.12.02.626511.

737 35. Huang, S., Piao, C., Beuschel, C.B., Zhao, Z., and Sigrist, S.J. (2022). A brain-wide
738 form of presynaptic active zone plasticity orchestrates resilience to brain aging in
739 Drosophila. PLOS Biol. *20*, e3001730. https://doi.org/10.1371/journal.pbio.3001730.

740 36. Huang, S., Piao, C., Beuschel, C.B., Götz, T., and Sigrist, S.J. (2020). Presynaptic
741 Active Zone Plasticity Encodes Sleep Need in Drosophila. Curr Biol *30*, 1077-1091.e5.
742 https://doi.org/10.1016/j.cub.2020.01.019.

743 37. Weiss, J.T., Blundell, M.Z., Singh, P., and Donlea, J.M. (2024). Sleep deprivation
744 drives brain-wide changes in cholinergic presynapse abundance in Drosophila
745 melanogaster. Proc. Natl. Acad. Sci. *121*, e2312664121.
746 https://doi.org/10.1073/pnas.2312664121.

747 38. Weiss, J.T., and Donlea, J.M. (2021). Sleep deprivation results in diverse patterns of
748 synaptic scaling across the Drosophila mushroom bodies. Curr. Biol. *31*, 3248-3261.e3.
749 https://doi.org/10.1016/j.cub.2021.05.018.

750 39. Gupta, V.K., Pech, U., Bhukel, A., Fulterer, A., Ender, A., Mauermann, S.F.,
751 Andlauer, T.F.M., Antwi-Adjei, E., Beuschel, C., Thriene, K., et al. (2016). Spermidine
752 Suppresses Age-Associated Memory Impairment by Preventing Adverse Increase of

753 Presynaptic Active Zone Size and Release. Plos Biol *14*, e1002563.
754 https://doi.org/10.1371/journal.pbio.1002563.

755 40. Ghelani, T., Escher, M., Thomas, U., Esch, K., Lützkendorf, J., Depner, H.,
756 Maglione, M., Parutto, P., Gratz, S., Matkovic-Rachid, T., et al. (2023). Interactive
757 nanocluster compaction of the ELKS scaffold and Cacophony Ca2+ channels drives
758 sustained active zone potentiation. Sci. Adv. *9*, eade7804.
759 https://doi.org/10.1126/sciadv.ade7804.

760 41. Kiragasi, B., Wondolowski, J., Li, Y., and Dickman, D.K. (2017). A Presynaptic
761 Glutamate Receptor Subunit Confers Robustness to Neurotransmission and
762 Homeostatic Potentiation. Cell Reports *19*, 2694–2706.
763 https://doi.org/10.1016/j.celrep.2017.06.003.

764 42. Ermolyuk, Y.S., Alder, F.G., Surges, R., Pavlov, I.Y., Timofeeva, Y., Kullmann,
765 D.M., and Volynski, K.E. (2013). Differential triggering of spontaneous glutamate
766 release by P/Q-, N- and R-type Ca2+ channels. Nat. Neurosci. *16*, 1754–1763.
767 https://doi.org/10.1038/nn.3563.

768 43. Zirin, J., Hu, Y., Liu, L., Yang-Zhou, D., Colbeth, R., Yan, D., Ewen-Campen, B.,
769 Tao, R., Vogt, E., VanNest, S., et al. (2020). Large-Scale Transgenic Drosophila
770 Resource Collections for Loss- and Gain-of-Function Studies. Genetics *214*, 755–767.
771 https://doi.org/10.1534/genetics.119.302964.

772 44. Sun, H., Nishioka, T., Hiramatsu, S., Kondo, S., Amano, M., Kaibuchi, K., Ichinose,
773 T., and Tanimoto, H. (2020). Dopamine receptor Dop1R2 stabilizes appetitive olfactory
774 memory through the Raf/MAPK pathway in Drosophila. J Neurosci *40*, 1572–19.
775 https://doi.org/10.1523/jneurosci.1572-19.2020.

776 45. Busch, S., Selcho, M., Ito, K., and Tanimoto, H. (2009). A map of octopaminergic
777 neurons in the Drosophila brain. J Comp Neurol *513*, 643–667.
778 https://doi.org/10.1002/cne.21966.

779 46. Monastirioti, M., Jr., C.E.L., and White, K. (1996). Characterization of Drosophila
780 Tyramine β-HydroxylaseGene and Isolation of Mutant Flies Lacking Octopamine. J
781 Neurosci *16*, 3900–3911. https://doi.org/10.1523/jneurosci.16-12-03900.1996.

782 47. Dietzl, G., Chen, D., Schnorrer, F., Su, K.-C., Barinova, Y., Fellner, M., Gasser, B.,
783 Kinsey, K., Oppel, S., Scheiblauer, S., et al. (2007). A genome-wide transgenic RNAi
784 library for conditional gene inactivation in Drosophila. Nature *448*, 151–156.
785 https://doi.org/10.1038/nature05954.

786 48. Maqueira, B., Chatwin, H., and Evans, P.D. (2005). Identification and
787 characterization of a novel family of Drosophilaβ-adrenergic-like octopamine G-protein
788 coupled receptors. J Neurochem *94*, 547–560. https://doi.org/10.1111/j.1471-
789 4159.2005.03251.x.

790 49. Levin, L.R., Han, P.-L., Hwang, P.M., Feinstein, P.G., Davis, R.L., and Reed, R.R.
791 (1992). The Drosophila learning and memory gene rutabaga encodes a
792 Ca2+calmodulin-responsive adenylyl cyclase. Cell *68*, 479–489.
793 https://doi.org/10.1016/0092-8674(92)90185-f.

794 50. Livingstone, M.S., Sziber, P.P., and Quinn, W.G. (1984). Loss of
795 calcium/calmodulin responsiveness in adenylate cyclase of rutabaga, a Drosophila
796 learning mutant. Cell *37*, 205–215. https://doi.org/10.1016/0092-8674(84)90316-7.

797 51. Han, P.-L., Levin, L.R., Reed, R.R., and Davis, R.L. (1992). Preferential expression
798 of the drosophila rutabaga gene in mushroom bodies, neural centers for learning in
799 insects. Neuron *9*, 619–627. https://doi.org/10.1016/0896-6273(92)90026-a.

800 52. Thum, A.S., Jenett, A., Ito, K., Heisenberg, M., and Tanimoto, H. (2007). Multiple
801 Memory Traces for Olfactory Reward Learning in Drosophila. J Neurosci *27*, 11132–
802 11138. https://doi.org/10.1523/jneurosci.2712-07.2007.

803 53. Perkins, L.A., Holderbaum, L., Tao, R., Hu, Y., Sopko, R., McCall, K., Yang-Zhou,
804 D., Flockhart, I., Binari, R., Shim, H.-S., et al. (2015). The Transgenic RNAi Project at
805 Harvard Medical School: Resources and Validation. Genetics *201*, 843–852.
806 https://doi.org/10.1534/genetics.115.180208.

807 54. LeDue, E.E., Mann, K., Koch, E., Chu, B., Dakin, R., and Gordon, M.D. (2016).
808 Starvation-Induced Depotentiation of Bitter Taste in Drosophila. Curr Biol *26*, 2854–
809 2861. https://doi.org/10.1016/j.cub.2016.08.028.

810 55. Renger, J.J., Ueda, A., Atwood, H.L., Govind, C.K., and Wu, C.-F. (2000). Role of
811 cAMP Cascade in Synaptic Stability and Plasticity: Ultrastructural and Physiological
812 Analyses of Individual Synaptic Boutons in Drosophila Memory Mutants. J Neurosci
813 *20*, 3980–3992. https://doi.org/10.1523/jneurosci.20-11-03980.2000.

814 56. Boto, T., Louis, T., Jindachomthong, K., Jalink, K., and Tomchik, S.M. (2014).
815 Dopaminergic Modulation of cAMP Drives Nonlinear Plasticity across the Drosophila
816 Mushroom Body Lobes. Curr Biol *24*, 822–831.
817 https://doi.org/10.1016/j.cub.2014.03.021.

818 57. Wang, L., Wu, C., Peng, W., Zhou, Z., Zeng, J., Li, X., Yang, Y., Yu, S., Zou, Y.,
819 Huang, M., et al. (2022). A high-performance genetically encoded fluorescent indicator
820 for in vivo cAMP imaging. Nat. Commun. *13*, 5363. https://doi.org/10.1038/s41467-
821 022-32994-7.

822 58. Maiellaro, I., Lohse, M.J., Kittel, R.J., and Calebiro, D. (2016). cAMP Signals in
823 Drosophila Motor Neurons Are Confined to Single Synaptic Boutons. Cell Reports *17*,
824 1238–1246. https://doi.org/10.1016/j.celrep.2016.09.090.

825 59. Zaccolo, M., Zerio, A., and Lobo, M.J. (2021). Subcellular Organization of the
826 cAMP Signaling Pathway. Pharmacol. Rev. *73*, 278–309.
827 https://doi.org/10.1124/pharmrev.120.000086.

828 60. Gervasi, N., Tchénio, P., and Preat, T. (2010). PKA Dynamics in a Drosophila
829 Learning Center: Coincidence Detection by Rutabaga Adenylyl Cyclase and Spatial
830 Regulation by Dunce Phosphodiesterase. Neuron *65*, 516–529.
831 https://doi.org/10.1016/j.neuron.2010.01.014.

832 61. Ehmann, N., Owald, D., and Kittel, R.J. (2017). Drosophila active zones: From
833 molecules to behaviour. Neurosci Res *127*, 14–24.
834 https://doi.org/10.1016/j.neures.2017.11.015.

835 62. Cunningham, K.L., Sauvola, C.W., Tavana, S., and Littleton, J.T. (2022).
836 Regulation of presynaptic Ca2+ channel abundance at active zones through a balance of
837 delivery and turnover. eLife *11*, e78648. https://doi.org/10.7554/elife.78648.

838 63. Williams, C.L., and Smith, S.M. (2018). Calcium dependence of spontaneous
839 neurotransmitter release. J. Neurosci. Res. *96*, 335–347.
840 https://doi.org/10.1002/jnr.24116.

841 64. Handler, A., Graham, T.G.W., Cohn, R., Morantte, I., Siliciano, A.F., Zeng, J., Li,
842 Y., and Ruta, V. (2019). Distinct Dopamine Receptor Pathways Underlie the Temporal
843 Sensitivity of Associative Learning. Cell *178*, 60-75.e19.
844 https://doi.org/10.1016/j.cell.2019.05.040.

845 65. Noyes, N.C., and Davis, R.L. (2023). Innate and learned odor-guided behaviors
846 utilize distinct molecular signaling pathways in a shared dopaminergic circuit. Cell
847 Reports *42*, 112026. https://doi.org/10.1016/j.celrep.2023.112026.

848 66. Abe, T., Yamazaki, D., Hiroi, M., Ueoka, Y., Maeyama, Y., and Tabata, T. (2023).
849 Revisiting the role of cAMP in Drosophila aversive olfactory memory formation.
850 bioRxiv, 2023.06.26.545795. https://doi.org/10.1101/2023.06.26.545795.

851 67. Tsao, C.-H., Chen, C.-C., Lin, C.-H., Yang, H.-Y., and Lin, S. (2018). Drosophila
852 mushroom bodies integrate hunger and satiety signals to control innate food-seeking
853 behavior. Elife *7*, e35264. https://doi.org/10.7554/elife.35264.

854 68. Hancock, C.E., Rostami, V., Rachad, E.Y., Deimel, S.H., Nawrot, M.P., and Fiala,
855 A. (2022). Visualization of learning-induced synaptic plasticity in output neurons of the
856 Drosophila mushroom body γ-lobe. Sci. Rep. *12*, 10421.
857 https://doi.org/10.1038/s41598-022-14413-5.

858 69. Perisse, E., Owald, D., Barnstedt, O., Talbot, C.B., Huetteroth, W., and Waddell, S.
859 (2016). Aversive Learning and Appetitive Motivation Toggle Feed-Forward Inhibition
860 in the Drosophila Mushroom Body. Neuron *90*, 1086–1099.
861 https://doi.org/10.1016/j.neuron.2016.04.034.

70. Pavlowsky, A., Schor, J., Plaçais, P.-Y., and Preat, T. (2018). A GABAergic Feedback Shapes Dopaminergic Input on the Drosophila Mushroom Body to Promote Appetitive Long-Term Memory. Curr Biol *28*, 1783-1793.e4. https://doi.org/10.1016/j.cub.2018.04.040.

71. Sitaraman, D., Aso, Y., Jin, X., Chen, N., Felix, M., Rubin, G.M., and Nitabach, M.N. (2015). Propagation of Homeostatic Sleep Signals by Segregated Synaptic Microcircuits of the Drosophila Mushroom Body. Curr. Biol. *25*, 2915–2927. https://doi.org/10.1016/j.cub.2015.09.017.

72. Berger, M., Auweiler, K., Tegtmeier, M., Dorn, K., Khadrawe, T.E., and Scholz, H. (2023). Octopamine integrates the status of internal energy supply into the formation of food-related memories. https://doi.org/10.7554/elife.88247.1.

73. Claßen, G., and Scholz, H. (2018). Octopamine Shifts the Behavioral Response From Indecision to Approach or Aversion in Drosophila melanogaster. Front Behav Neurosci *12*, 131. https://doi.org/10.3389/fnbeh.2018.00131.

74. Scheiner, R., Steinbach, A., Claßen, G., Strudthoff, N., and Scholz, H. (2014). Octopamine indirectly affects proboscis extension response habituation in Drosophila melanogaster by controlling sucrose responsiveness. J Insect Physiol *69*, 107–117. https://doi.org/10.1016/j.jinsphys.2014.03.011.

75. Schneider, A., Ruppert, M., Hendrich, O., Giang, T., Ogueta, M., Hampel, S., Vollbach, M., Büschges, A., and Scholz, H. (2012). Neuronal Basis of Innate Olfactory Attraction to Ethanol in Drosophila. Plos One *7*, e52007. https://doi.org/10.1371/journal.pone.0052007.

76. Yang, Z., Yu, Y., Zhang, V., Tian, Y., Qi, W., and Wang, L. (2015). Octopamine mediates starvation-induced hyperactivity in adult Drosophila. Proc National Acad Sci *112*, 5219–5224. https://doi.org/10.1073/pnas.1417838112.

77. Youn, H., Kirkhart, C., Chia, J., and Scott, K. (2018). A subset of octopaminergic neurons that promotes feeding initiation in Drosophila melanogaster. Plos One *13*, e0198362. https://doi.org/10.1371/journal.pone.0198362.

78. Sayin, S., Backer, J.-F.D., Siju, K.P., Wosniack, M.E., Lewis, L.P., Frisch, L.-M., Gansen, B., Schlegel, P., Edmondson-Stait, A., Sharifi, N., et al. (2019). A Neural Circuit Arbitrates between Persistence and Withdrawal in Hungry Drosophila. Neuron *104*, 544-558.e6. https://doi.org/10.1016/j.neuron.2019.07.028.

79. Turrel, O., Ramesh, N., Escher, M.J.F., Pooryasin, A., and Sigrist, S.J. (2022). Transient active zone remodeling in the Drosophila mushroom body supports memory. Curr Biol. https://doi.org/10.1016/j.cub.2022.10.017.

80. Zhang, X., Li, Q., Wang, L., Liu, Z.-J., and Zhong, Y. (2018). Active Protection: Learning-Activated Raf/MAPK Activity Protects Labile Memory from Rac1-

Independent Forgetting. Neuron *98*, 142-155.e4. https://doi.org/10.1016/j.neuron.2018.02.025.

81. Sage, D., Donati, L., Soulez, F., Fortun, D., Schmit, G., Seitz, A., Guiet, R., Vonesch, C., and Unser, M. (2017). DeconvolutionLab2: An open-source software for deconvolution microscopy. Methods *115*, 28–41. https://doi.org/10.1016/j.ymeth.2016.12.015.

82. Haase, R., Royer, L.A., Steinbach, P., Schmidt, D., Dibrov, A., Schmidt, U., Weigert, M., Maghelli, N., Tomancak, P., Jug, F., et al. (2020). CLIJ: GPU-accelerated image processing for everyone. Nat. Methods *17*, 5–6. https://doi.org/10.1038/s41592-019-0650-1.

83. Ollion, J., Cochennec, J., Loll, F., Escudé, C., and Boudier, T. (2013). TANGO: a generic tool for high-throughput 3D image analysis for studying nuclear organization. Bioinformatics *29*, 1840–1841. https://doi.org/10.1093/bioinformatics/btt276.

84. Kondo, S., and Ueda, R. (2013). Highly Improved Gene Targeting by Germline-Specific Cas9 Expression in Drosophila. Genetics *195*, 715–721. https://doi.org/10.1534/genetics.113.156737.

85. Ke, M.-T., Nakai, Y., Fujimoto, S., Takayama, R., Yoshida, S., Kitajima, T.S., Sato, M., and Imai, T. (2016). Super-Resolution Mapping of Neuronal Circuitry With an Index-Optimized Clearing Agent. Cell Reports *14*, 2718–2732. https://doi.org/10.1016/j.celrep.2016.02.057.

86. Yamagata, N., Ezaki, T., Takahashi, T., Wu, H., and Tanimoto, H. (2021). Presynaptic inhibition of dopamine neurons controls optimistic bias. Elife *10*, e64907. https://doi.org/10.7554/elife.64907.